Chapter 6

Nodal-line symmetry breaking induced colossal anomalous Hall and Nernst effects in Cu_2CoSn Heusler compound

This work is authored by Gaurav K. Shukla et al. and published in Appl. Phys. Lett. 123, 052402 (2023).

In this chapter, the anomalous Hall and Nernst effect in the Cu_2CoSn Heusler compound have been studied using theoretical calculations. We found the nodal lines lie very close to the Fermi level. The nodal lines are gapped out due to the spin-orbit coupling (SOC) and create substantial Berry curvature around it. The Berry curvature calculation gives a large anomalous Hall conductivity (AHC) of about 1000 S/cm and anomalous Nernst conductivity (ANC) of about 3.98 A/m-K due to the large Berry curvature at the Fermi surface.

6.1 Introduction

In the preceding chapters, we extensively explored the anomalous Hall effect (AHE) in different Co-based Heusler compounds. Anomalous Nernst effect (ANE); another interesting phenomenon that is a counterpart of AHE describes the generation of transverse voltage drop in the material with broken time-reversal symmetry (TRS) when subjected to a longitudinal temperature gradient [1, 2, 62]. The ANE is closely analogous to the AHE *i.e.* ANE also arises from intrinsic and extrinsic contributions [2, 4]. Several experimental, as well as theoretical studies on ANE, have been reported on magnetic materials [2, 6–8, 63]. The discovery of topological materials simulated significant interest in condensed matter physics for their unique electronic properties and potential for technological applications [9–12]. Among these materials, topological semimetals (TSMs) have emerged as a particularly intriguing class of gapless electronic phases exhibiting topologically protected stable crossings of energy bands [9, 10]. The Dirac semimetal, a category of TSMs exhibits a four-fold degeneracy at the Dirac point, while Weyl semimetals (WSMs), which are a subset of Dirac semimetals, arise when inversion and/or time-reversal symmetry is broken, leading to the formation of Weyl points and the lifting of this degeneracy [13–16]. WSMs show a variety of interesting phenomena such as chiral anomaly, chiral magnetotransport, and anomalous transport response owing to their unique band topology [17–26]. WSMs have been extensively discovered as a consequence of breaking inversion symmetry (IS) [19–23]. More recently, a new class of WSMs, known as magnetic WSMs, have been identified arising from the breaking of TRS [24, 25]. The notable advantage of magnetic WSMs over conventional WSMs is their susceptibility to easy manipulation of band topology by controlling the direction of the magnetic moment [24, 26]. Besides the zero dimension crossing of bands in the WSMs, the higher dimension crossing is also possible,

where the bands cross each other along a closed curve called nodal lines (NLs) [27, 28]. These NLs are generally protected by the certain symmetry of the crystal. E.g., the TRS and IS can protect the NLs in the absence of spin-orbit coupling (SOC) [29, 30]. The mirror symmetries with opposite eigenvalues can also protect the NLs both in the presence and absence of SOC [31–33]. WSMs are prominent materials for the large AHE and ANE as the Weyl points in the momentum space act as the magnetic monopole and are the source and drain of the Berry curvature [2, 34]. Besides the Weyl points, if the NLs present in the *k*-space gap out due to SOC, the Berry curvature introduces along the gapped NLs and creates the transverse voltage in the system [2, 34]. If the Weyl points or gapped NLs are near the Fermi level their signatures can be observed in the anomalous transport properties of materials [25, 35]. For *e.g.*, the first discovered magnetic WSMs $Co_3Sn_2S_2$ shows the large anomalous Hall conductivity (AHC) due to the gapped NLs and the Weyl points present in the system [35]. The ANE in the $Co_3Sn_2S_2$, Mn_3X (X = Ge, Sn) and Fe_3X (X = Ga, Al) are interesting due to their characteristic low-energy electronics structure including Weyl points near to the Fermi energy [6–8, 63]. Among the different classes of materials, Heusler compounds are promising for their wide range of properties [36–38]. Recently, Heusler compounds attracted much interest as quantum material because some of them are discovered as magnetic WSM due to the co-existence of the magnetism and the topology [2, 24–26, 39]. Heusler compounds also promise the large AHE and ANE due to large Berry curvature associated with their topological band structure [2, 40]. The largest AHC ($\sim$ 1260 S/cm [2] and 2000 S/cm at 2T [41]) and anomalous Nernst conductivity (ANC) ($\sim$ 4 A/m-k [41]) so far, reported in the Co_2MnGa magnetic Heusler compound.

Cu_2CoSn Heusler compound has been identified as the topological semimetal in the topological material database and expected to exhibit large AHC [42–44]. In the present work, we theoretically investigated the structural, magnetic, and anomalous transport properties in the Cu_2CoSn Heusler compound. Cu_2CoSn is a ferromagnetic material, which exhibits the NLs at the Fermi level, that are protected by the mirror symmetry of the lattice. Upon introducing the SOC in the Hamiltonian and by setting the magnetization axis along [001] direction, we found the NLs gapped out and the large Berry curvature appears over the Fermi surface, which results in the large AHC and ANC in the system. The Berry curvature calculation gives the AHC and ANC around $\sim$1000 S/cm and $\sim$ 3.98 A/m-K at the Fermi level, which is comparable to the largest reported AHC and ANC in the

well known Co_2MnGa Heusler compound [2].

6.2 Computational details

The *ab initio* calculation for the electronic band structure of Cu_2CoSn was performed by employing the density functional theory using the Quantum Espresso code [45]. The Plane wave basis set and the Optimized norm-conserving Vanderbilt pseudo-potentials [46] were used for the calculation. The plane wave cutoff energy was chosen at 80 Ry and the exchange-correlation functional was chosen in the generalized gradient approximation [47]. The integration in k-space was carried out with $8\times8\times8$ grid and the convergence criterion of total energy was chosen 10^{-8} eV. We extracted the Wannier functions from the DFT bands by Wannier90 code [48, 49]. The maximally localized Wannier functions (MLWFs) for p orbitals on Sn and p_z, d orbitals on Cu and s, p_z, and d orbitals on Co have been used as the basis of the tight-binding Hamiltonian. The Kubo formula implemented in the Wannier90 code was used for the calculation of the Berry curvature, which can be given as [50]

$$\Omega_{ij}^{n} = i\sum_{n\neq n'}\frac{\langle n|\frac{\partial H}{\partial R^i}|n'\rangle\langle n'|\frac{\partial H}{\partial R^j}|n\rangle - (i\leftrightarrow j)}{(E_n - E_n')^2} \tag{6.1}$$

Here E_n and $|n\rangle$ are the eigenvalue and eigenstate of the Hamiltonian H.

The AHC can be calculated using the equation;

$$\sigma_{ij} = -\frac{e^2}{\hbar}\sum_{n}\int\frac{d^3k}{(2\pi)^3}\Omega_{ij}^{n}f_n. \tag{6.2}$$

Here, f_n represents the Fermi distribution function. The expression for ANC can be given as [2];

$$\alpha_{ij}^{A}(T,\mu) = -\frac{1}{T}\frac{e}{\hbar}\sum_{n}\int\frac{d^3k}{(2\pi)^3}\Omega_{ij}^{n}[(E_n-\mu)f_n + K_BT\,ln(1+exp(-\frac{E_n-\mu}{K_BT}))]. \tag{6.3}$$

Near zero temperature, the above equation can be written as

$$\frac{\alpha_{ij}^{A}}{T} = -\frac{\pi^2}{3}\frac{K_B^2}{e}\frac{d\sigma_{\mathrm{ij}}}{d\mu} \tag{6.4}$$

where α_{ij}^{A}, K_B, σ_{ij} and μ are the ANC, Boltzmann constant, AHC, and chemical potential, respectively.

6.3 Result and discussion

We investigated the Cu_2CoSn regular full Heusler compound with space group $Fm\bar{3}m$ and the unit cell of the compound is shown in Fig. 6.1(a). The special Wyckoff's positions 8c (0.25, 0.25, 0.25), 4b (0.5, 0.5,0.5), and 4a (0, 0, 0) were considered for Cu, Co, and Sn atoms, respectively. The crystal structure has space inversion symmetry with three perpendicular relevant mirror planes. Figure 6.1(b) shows the energy versus lattice parameter curve, which suggests the lattice parameter a = b = c = 6.05 Å for the present system. The compound is ferromagnetic with a magnetic moment of 1.15

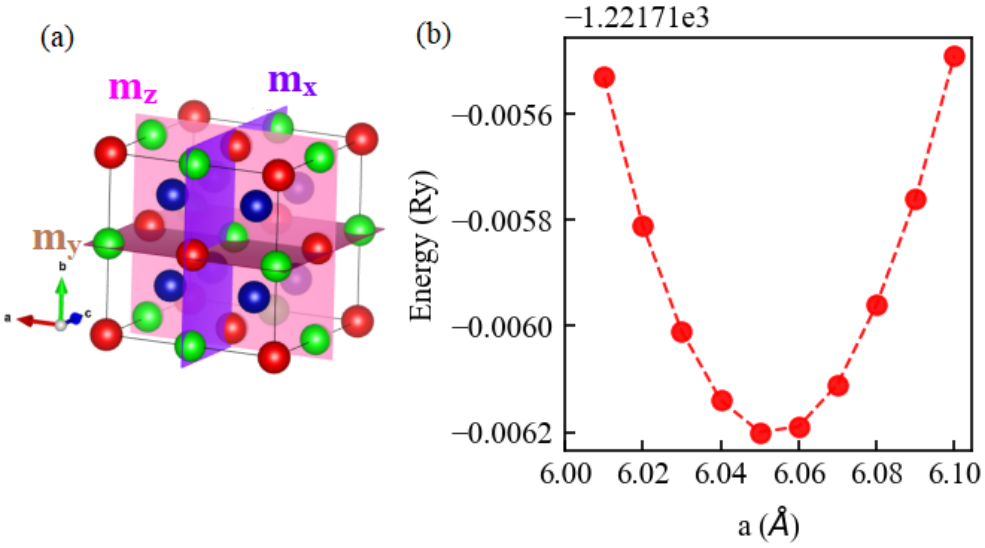

Figure 6.1: (a) An unit cell of Cu_2CoSn Heusler compound. Blue, red, and green colors represent the Cu, Co, and Sn atoms, respectively. Three perpendicular mirror planes are designated as m_x, m_y, and m_z, respectively. (b) Energy versus lattice parameter curve for the Cu_2CoSn Heusler compound.

μ_B per formula of the unit cell. The cobalt atom contributes exclusively to the magnetization (μ_{Co} = 1.147 μ_B/f.u.) as Cu and Sn are the non-magnetic elements. The non-integer magnetic moment suggests that the system deviates from the half-metallic behavior. In the absence of SOC, the crys-

tal symmetry of magnetic Cu_2CoSn full Heusler compound belongs to space group $Fm\bar{3}m$, which exhibits three relevant mirror reflection symmetries m_x=0, m_y=0 and m_z=0 in the planes k_x=0, k_y=0 and k_z=0, respectively [25, 51, 52]. In each of these planes, there is a mirror symmetry protected NL in the Brillouin zone derived from the opposite eigenvalue of mirror symmetries and cross each other at six distinct points [26, 51, 52]. These NLs gap out in the presence of SOC according to the magnetization direction, e.g., if the magnetization is considered along [001] direction, then the mirror symmetries m_x and m_y are no longer remain symmetry planes, while the m_z remains the symmetry plane, as the z-component of the spin S_z is left invariant by m_z. Therefore, the NL in the k_x = 0 and k_y = 0 planes gap out, while the NL in the k_z=0 remain still protected by the mirror reflection symmetry. The total outward Berry flux from the gapless NL is zero, while the gapped NLs produce the non-zero Berry flux in the surrounding area [25, 53]. The NLs in the k_x = 0 and k_y = 0 planes gapped out due to SOC result into the band anti-crossings, which restricts the Berry curvature to be aligned in magnetization direction [54].

Figure 6.2(a) represents the Brillouin zone of the FCC lattice with high-symmetry lines and points. The spin-polarized band structure of Cu_2CoSn along high-symmetry k path X (0.5, 0, 0.5)-Γ (0, 0, 0)-L (0.5, 0.5, 0.5)-W (0.50, 0.25, 0.75)-K (0.375, 0.375, 0.750) -Γ (0, 0, 0) in the k_z=0 plane is shown Fig. 6.2(b). Noteworthy, the coordinates of high-symmetry point L remain the same regardless of the chosen plane. The red and blue colors represent the majority and minority states, respectively. Two crossings; one is made from the crossing of the majority and minority spin states (say A) and another between minority spin states (say B) at the Fermi level along the K-Γ direction [inset of Fig. 6.2(b)] seems a feature of interest in the band structure as there is a possibility of the formation of NL in the Brillouin zone. Since SOC plays a pivotal role in realizing the anomalous transport in materials and is also ubiquitous in materials with $3d$ elements [25], therefore it is necessary to study the band structure with non-vanishing SOC. The band structure in the presence of SOC in the k_z=0 plane of the Brillouin zone is shown in Fig. 6.2(c). The crossing points A and B are still intact with SOC [inset of Fig. 6.2(c)], which indicates that crossings (NLs) are still protected by the m_z mirror reflection symmetry of the lattice. Now, we plotted the SOC band structure of the Cu_2CoSn along the high-symmetry k path *X'* (0, 0.5, 0.5)-Γ (0, 0, 0)-L (0.5, 0.5, 0.5)-*W'* (0.75, 0.25, 0.50)-*K'* (0.750, 0.375, 0.375)-Γ (0, 0, 0) in the k_x =0 plane as shown in Fig. 6.2(d). The degener-

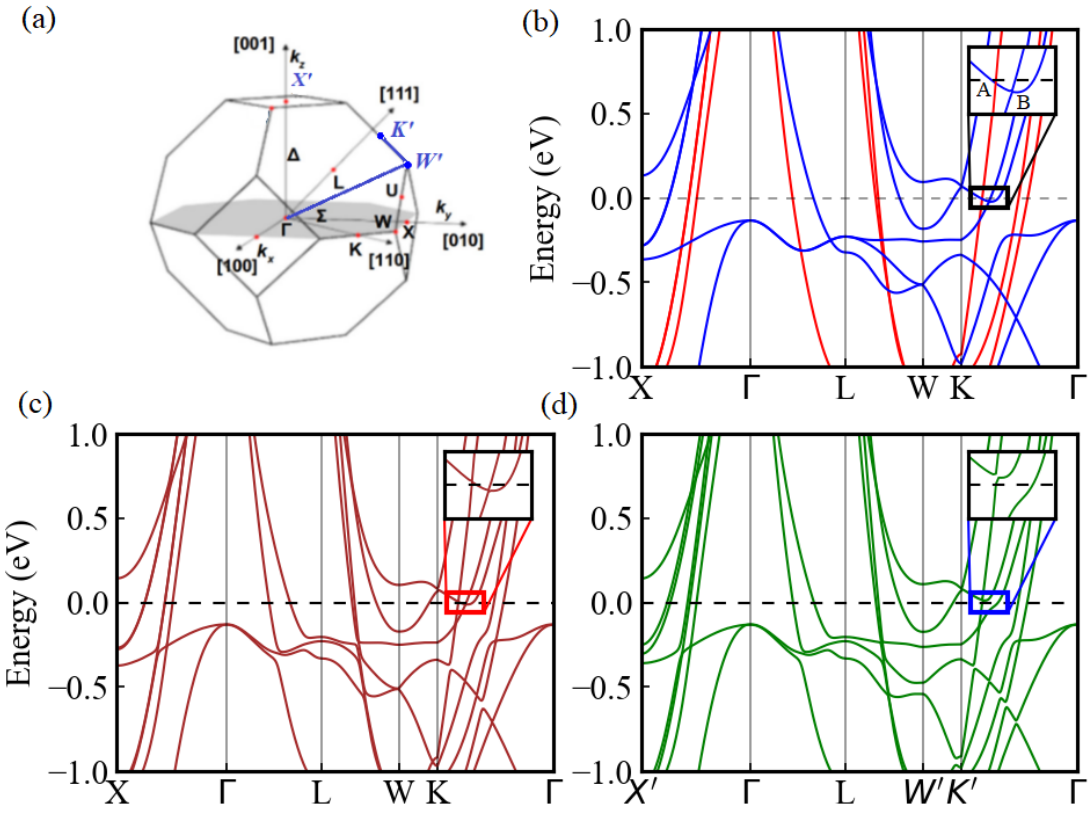

Figure 6.2: (a) A Brillouin zone of the face-centered cubic lattice with high-symmetry points and lines. (b) Spin-polarized band structure (spin-up: red; spin-down: blue) in k_z =0 plane. (c) Band structure with spin-orbit coupling (SOC) in the k_z =0 plane. (d) Band structure with SOC in k_x =0 plane. The inset of (b),(c), and (d) show an enlarged view around the crossing points A and B along the K- Γ direction.

acy of crossing point A lost due to SOC in the k_x=0 plane and hence a gap of 7 meV opens at the crossing point because k_x =0 plane no longer remains the symmetry of plane when magnetization is along [001] direction. The crossing point B also no longer persists due to SOC and disappears. The zoom view around the crossing points A and B is shown in the inset of Fig.6.2(d). To calculate the topological properties for *e.g.* Berry curvature, AHC, and ANC, etc., we constructed the MLWF from the Bloch states using Wannier90 code and found a good match between the electronic and Wannier interpolated band structure. The Wannier interpolation is an effective tool to calculate the *k*-space integrals, which are involved in finding out several properties of materials such as AHC, ANC, spin Hall conductivity, optical properties, etc [48, 49, 55]. To visualize the NLs in the Brillouin zone, we plotted the band gaps corresponding to the band crossings A and B in the two-dimensional Brillouin zone on two different *k*-planes. Figure 6.3(a-i) shows the energy gap of crossing A in the k_z = 0 plane, in which mirror symmetry (m_z) is preserved even in the presence of

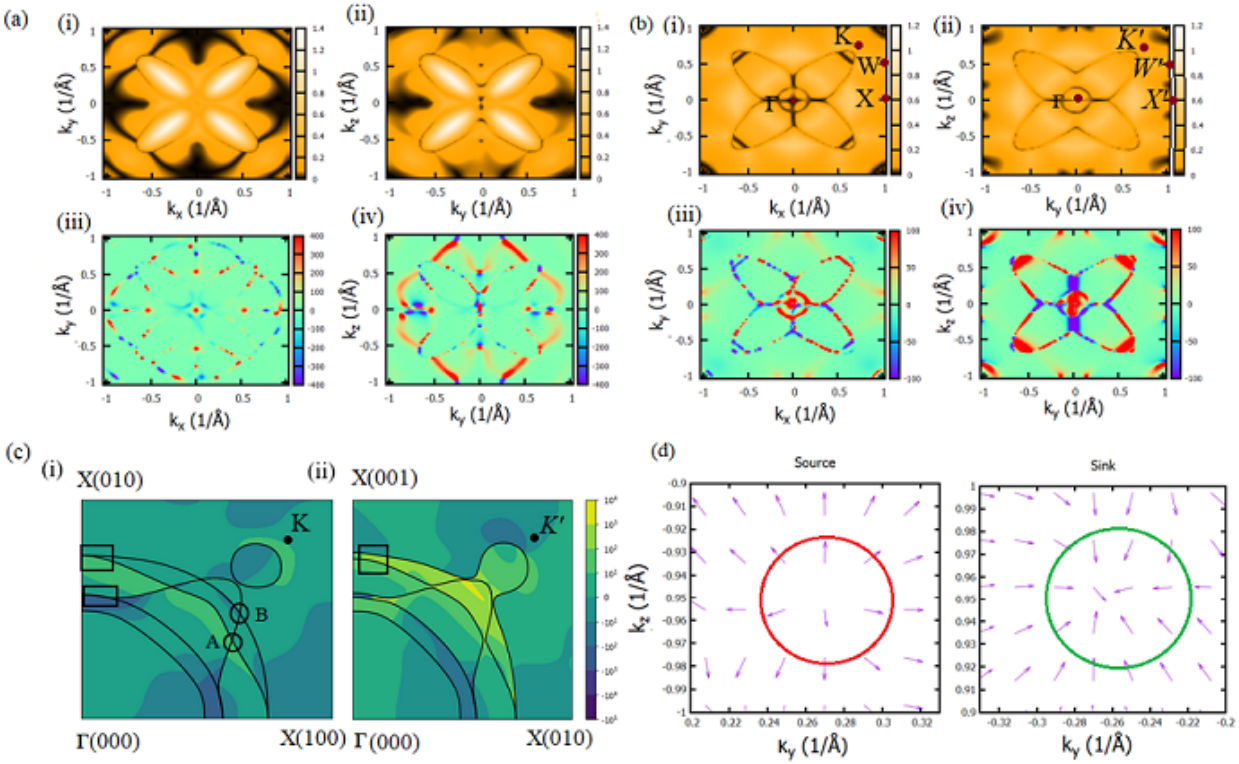

Figure 6.3: (a) and (b) The energy gap in (i) k_z = 0 plane (ii) k_x = 0 plane and Berry curvature distribution in the (iii) k_z =0 plane (iv) k_x =0 plane, for crossings A and B, respectively. The black color in (i) and (ii) represents the vanishing energy gap of the bands. (c) Fermi surface (solid lines) and Berry curvature (color map) in the (i) k_z = 0 plane (ii) k_x = 0 plane. (d) The normalized Berry curvature for the Weyl points in k_x = 0 plane. The Weyl points act as the source and drain of the Berry flux.

SOC. As a consequence, a closed NL is observed in this plane as shown in the black color, which is protected by the m_z mirror reflection symmetry. The Berry curvature was calculated in the same k_z = 0 plane as presented in Fig. 6.3(a-iii), which shows that the Berry curvature around the preserved NL is very weak. It is interesting to look at the NL and Berry curvature in the k_x = 0 plane, which is not a plane of symmetry after considering the SOC and the magnetization direction. The NL, which was preserved in the k_z = 0 plane, gapped out in the k_x = 0 plane (Fig. 6.3(a-ii)), because of the mirror symmetry in this plane breaks upon considering the SOC and magnetization direction. The Berry curvature distribution in the same k_x = 0 planes is shown in Fig. 6.3(a-iv). As expected, a strong Berry curvature induces along the gapped NL, which can manifest a large transverse response in the system. A similar kind of NL and the Berry curvature is also expected in the k_y = 0 plane. Similarly, we have also plotted the energy gap and Berry curvature for crossing B in the k_z = 0 and k_x = 0 planes as shown in Figs. 6.3(b-i)-6.3(b-iv). The closed gap along the Γ-K direction

(in $k_z = 0$ plane) disappears in the $k_x = 0$ plane and the Berry curvature appears at the gapped line. Huyen *et.al.* studied the AHE in the antiferromagnetic manganese nitrides and found that despite having a lower number of Weyl points around the Fermi level the AHC is highest in Mn_3PtN due to large Berry curvature at the Fermi surface originated from the high SOC of Pt element [56]. We have also analyzed the Fermi surface of Cu_2CoSn along with the Berry curvature for the present system. Fig. 6.3(c-i) shows the Fermi contours on the mirror plane at $k_z = 0$ with SOC. Along the Γ-X(010) direction, we found three Fermi lines out of them two are degenerate (shown inside rectangular bracket), and also two Fermi crossings (NLs) which are shown inside the circle. In the Fermi contour on $k_z = 0$ plane, the negligible Berry curvature is found to be associated with the Fermi lines. We plotted the same Fermi contour in $k_x = 0$ plane with SOC as shown in Fig. 6.3(c-ii). We observed that at one of the crossing points (crossing A) a tiny gap opens and another Fermi line (crossing B) disappears from the contour due to which a large Berry curvature emerges at the Fermi surface. Also, a small Berry curvature arises from the lifted degeneracy of the bands along the Γ-X(010) direction as shown inside the rectangle of Fig. 6.3(c-ii). Therefore the gapped NLs at the Fermi-energy is the main source of Berry curvature in the system.

Since the mirror symmetry is broken in both $k_y = 0$ and $k_x = 0$ planes upon considering SOC and [001] magnetization, hence the Weyl points can only emerge in these planes. The mirror symmetry is still preserved in $k_z = 0$ planes, therefore the Weyl point cannot be in the $k_z = 0$ plane. Noteworthy, these Weyl points do not exist in the system naturally due to SOC but rather derived from the NLs, because at some k-points the NLs refuse to break out [26, 39]. The Berry curvature due to Weyl points derived from the gapped NL is typically small as sometimes they lie far away from the Fermi level and/or due to other Weyl points present in the same plane [26, 39]. The energy and momentum space location of the Weyl points due to the breaking of NL in possible k-planes are mentioned in Table 6.1.

To further confirm the obtained points as the Weyl points, we plotted the normalized Berry curvature enclosing the coordinates of the Weyl points in k_x=0 plane [Fig. 6.3(d)]. We found that the Weyl point of chirality + 1 acts as a source of Berry curvature [outward flux in Fig. 6.3(d)] and the Weyl point with chirality -1 acts as a sink of Berry curvature [inward flux in Fig. 6.3(d)]. The emerging Berry curvature due to the gapped NLs at the Fermi level is supposed to create the large AHC in

Weyl point	k_x (2π/a)	k_y (2π/a)	k_z(2π/a)	E (eV)
$W_{\pm A}$	0.26	0.00	$\pm$0.95	-0.240
$W_{\pm B}$	0.00	$\pm$0.26	$\mp$0.95	0.235
$W_{\pm C}$	0.00	0.00	$\pm$0.51	0.73

Table 6.1: Representative coordinates of Weyl points in different planes in the momentum space with their chemical potentials concerning the Fermi energy.

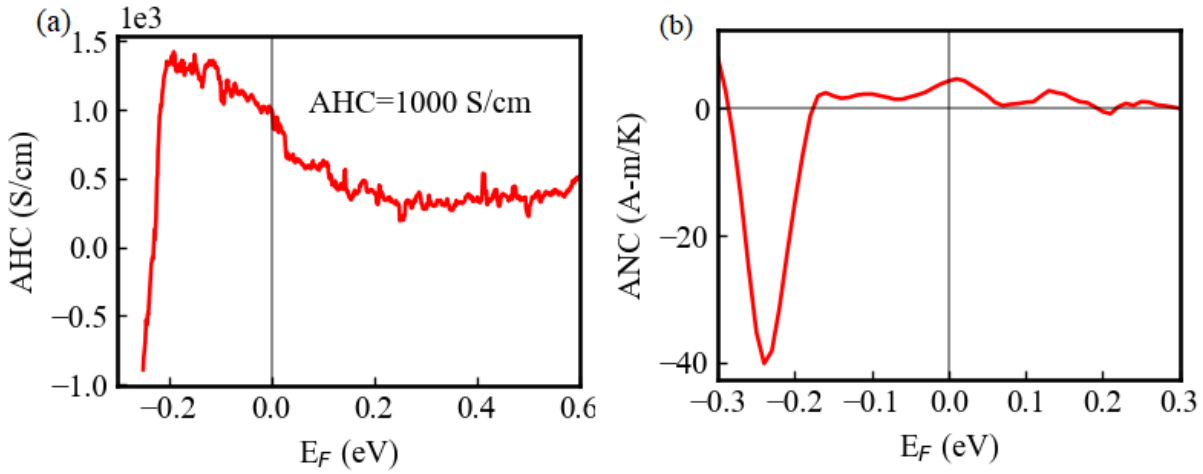

Figure 6.4: (a) Fermi-level dependent (a) Anomalous Hall conductivity. (b) Anomalous Nernst conductivity.

the material. For this, we calculated the AHC by the integration of Berry curvature of all occupied dispersion bands using Eq.6.1 and Eq.6.2. In the underlying space group with the magnetization along [001] direction, the Berry curvature pseudo-vector follows the relation [57];

$$\begin{aligned} \Omega_x(k_x, k_y, -k_z) &= -\Omega_x(k_x, k_y, k_z) \\ \Omega_y(k_x, k_y, -k_z) &= -\Omega_y(k_x, k_y, k_z) \\ \Omega_z(k_x, k_y, -k_z) &= \Omega_z(k_x, k_y, k_z), \end{aligned} \tag{6.5}$$

which forces $\Omega_x = \Omega_y = 0$. Therefore, the z-component of AHC σ_z^A is unrestricted, while σ_x^A and σ_y^A identically vanish. The variation of AHC with Fermi energy is shown in Fig. 6.4 (a). We found the giant intrinsic AHC (σ_z^A) about 1003 S/cm at the Fermi energy, which varies to 1120 S/cm just 0.05 eV below the Fermi level. This magnitude of AHC is larger than most of the investigated systems [25, 58–60, 62, 63] and comparable to the highest AHC reported for Co_2MnGa Heusler compound [2, 41].

Now we will discuss the ANE in the present compound. The ANE is the thermoelectric counterpart of AHE, where the temperature gradient is used for the motion of charges instead of the electric field [61]. The origin of ANE is closely related to the AHE and the key difference is that the AHE is the summation of the Berry curvature over all occupied states, while the ANE is the sum of the Berry curvature of states close to the Fermi energy *i.e* the ANC is the sum of the Berry curvature on the Fermi surface [52, 61]. The magnitude of ANC is related to the variation of the AHC near the Fermi energy. The strong Berry curvature on the Fermi surface gives the $\frac{\alpha^A}{T}$ = 0.013 A/m-K^2 and hence the ANC reaches the $\sim$ 3.98 A/m-K at 300 K, which is similar to the highest reported value of ANC is 4.0 A/m-K in the Co_2MnGa experimentally. The variation of the ANC with the Fermi energy is shown in Fig. 6.4 (b). The large ANC value of about 40 A/m-K below 250 meV of the Fermi energy might be due to the flat band at this energy level. The flat band is a known route to produce the large anomalous Nernst effect in the material [62, 63].

6.4 Conclusion

In conclusion, we theoretically investigated the electronic, magnetic, and anomalous transport properties of Cu_2CoSn full Heusler compound. We have shown that the gapped NLs at the Fermi energy lead to the large AHC and ANC in the system. Therefore, the Cu_2CoSn is added as a new candidate in the family of Heusler compounds with high AHC and ANC. This work provides a comprehensive understanding of the anomalous transport properties in the NL hosting magnetic materials and motivates the further exploration of the Cu_2CoSn Heusler compound through experimental studies.

References

[1] M. Ikhlas, T. Tomita, T. Koretsune, M.-T. Suzuki, D. Nishio-Hamane, R. Arita, Y. Otani, and S. Nakatsuji, Large anomalous Nernst effect at room temperature in a chiral antiferromagnet, Nat. Phys. **13**, 1085 (2017).

[2] S. N. Guin, K. Manna, J. Noky, S. J. Watzman, C. Fu, N. Kumar, W. Schnelle, C. Shekhar, Y. Sun, J. Gooth, *et al.*, Anomalous Nernst effect beyond the magnetization scaling relation in the ferromagnetic Heusler compound Co_2MnGa, NPG Asia Mater. **11**, 16 (2019).

[62] T. Asaba, V. Ivanov, S. Thomas, S. Savrasov, J. Thompson, E. Bauer, and F. Ronning, Colossal anomalous Nernst effect in a correlated noncentrosymmetric kagome ferromagnet, Sci. Adv. **7**, eabf1467 (2021).

[4] M. Mizuguchi and S. Nakatsuji, Energy-harvesting materials based on the anomalous Nernst effect, Sci. Technol. Adv. Mater. **20**, 262 (2019).

[63] T. Chen, S. Minami, A. Sakai, Y. Wang, Z. Feng, T. Nomoto, M. Hirayama, R. Ishii, T. Koretsune, R. Arita, *et al.*, Large anomalous Nernst effect and nodal plane in an iron-based kagome ferromagnet, Sci. Adv. **8**, eabk1480 (2022).

[6] A. Sakai, S. Minami, T. Koretsune, T. Chen, T. Higo, Y. Wang, T. Nomoto, M. Hirayama, S. Miwa, D. Nishio-Hamane, *et al.*, Iron-based binary ferromagnets for transverse thermoelectric conversion, Nature **581**, 53 (2020).

[7] H. Yang, W. You, J. Wang, J. Huang, C. Xi, X. Xu, C. Cao, M. Tian, Z.-A. Xu, J. Dai, and Y. Li, Giant anomalous Nernst effect in the magnetic Weyl semimetal $Co_3Sn_2S_2$, Phys. Rev. Materials **4**, 024202 (2020).

[8] G.-Y. Guo and T.-C. Wang, Large anomalous Nernst and spin Nernst effects in the noncollinear antiferromagnets Mn_3X (X= Sn, Ge, Ga), Physical Review B **96**, 224415 (2017).

[9] S. Wang, B.-C. Lin, A.-Q. Wang, D.-P. Yu, and Z.-M. Liao, Quantum transport in Dirac and Weyl semimetals: A review, Adv. Phys.: X **2**, 518 (2017).

[10] M. Z. Hasan, G. Chang, I. Belopolski, G. Bian, S.-Y. Xu, and J.-X. Yin, Weyl, Dirac and high-fold chiral fermions in topological quantum matter, Nat. Rev. Mater. **6**, 784 (2021).

[11] A. H. Castro Neto, F. Guinea, N. M. R. Peres, K. S. Novoselov, and A. K. Geim, The electronic properties of graphene, Rev. Mod. Phys. **81**, 109 (2009).

[12] M. Z. Hasan and C. L. Kane, Colloquium: Topological insulators, Rev. Mod. Phys. **82**, 3045 (2010).

[13] O. Vafek and A. Vishwanath, Dirac fermions in solids: From high-T_c cuprates and graphene to topological insulators and Weyl semimetals, Annu. Rev. Condens. Matter Phys. **5**, 83 (2014).

[14] H. Weyl, *Gesammelte Abhandlungen: Band 1 bis 4*, Vol. 4 (Springer-Verlag, 1968).

[15] A. Burkov, Topological semimetals, Nat. Mater. **15**, 1145 (2016).

[16] M. Z. Hasan, S.-Y. Xu, I. Belopolski, and S.-M. Huang, Discovery of Weyl fermion semimetals and topological Fermi arc states, Annu. Rev. Condens. Matter Phys. **8**, 289 (2017).

[17] N. P. Armitage, E. J. Mele, and A. Vishwanath, Weyl and Dirac semimetals in three-dimensional solids, Rev. Mod. Phys. **90**, 015001 (2018).

[18] B. Yan and C. Felser, Topological materials: Weyl semimetals, Annu. Rev. Condens. Matter Phys. **8**, 337 (2017).

[19] S.-Y. Xu, I. Belopolski, N. Alidoust, M. Neupane, G. Bian, C. Zhang, R. Sankar, G. Chang, Z. Yuan, C.-C. Lee, *et al.*, Discovery of a Weyl Fermion semimetal and topological Fermi arcs, Science **349**, 613 (2015).

[20] L. Yang, Z. Liu, Y. Sun, H. Peng, H. Yang, T. Zhang, B. Zhou, Y. Zhang, Y. Guo, M. Rahn, *et al.*, Weyl semimetal phase in the non-centrosymmetric compound TaAs, Nat. Phys. **11**, 728 (2015).

[21] B. Lv, N. Xu, H. Weng, J. Ma, P. Richard, X. Huang, L. Zhao, G. Chen, C. Matt, F. Bisti, *et al.*, Observation of Weyl nodes in TaAs, Nat. Phys. **11**, 724 (2015).

[22] Y. Sun, Y. Zhang, C. Felser, and B. Yan, Strong intrinsic spin Hall effect in the TaAs family of Weyl semimetals, Phys. Rev. Lett. **117**, 146403 (2016).

[23] S.-Y. Xu, I. Belopolski, D. S. Sanchez, C. Zhang, G. Chang, C. Guo, G. Bian, Z. Yuan, H. Lu, T.-R. Chang, *et al.*, Experimental discovery of a topological Weyl semimetal state in TaP, Sci. Adv. **1**, e1501092 (2015).

[24] P. Chaudhary, K. K. Dubey, G. K. Shukla, S. Singh, S. Sadhukhan, S. Kanungo, A. K. Jena, S.-C. Lee, S. Bhattacharjee, J. Minár, and S. W. D'Souza, Role of chemical disorder in tuning the Weyl points in Vanadium doped Co_2TiSn, Phys. Rev. Mater. **5**, 124201 (2021).

[25] G. K. Shukla, J. Sau, N. Shahi, A. K. Singh, M. Kumar, and S. Singh, Anomalous Hall effect from gapped nodal line in the Co_2FeGe Heusler compound, Phys. Rev. B **104**, 195108 (2021).

[26] Z. Wang, M. G. Vergniory, S. Kushwaha, M. Hirschberger, E. V. Chulkov, A. Ernst, N. P. Ong, R. J. Cava, and B. A. Bernevig, Time-reversal-breaking Weyl fermions in magnetic Heusler alloys, Phys. Rev. Lett. **117**, 236401 (2016).

[27] A. Burkov, M. Hook, and L. Balents, Topological nodal semimetals, Phys. Rev. B **84**, 235126 (2011).

[28] M. Phillips and V. Aji, Tunable line node semimetals, Phys. Rev. B **90**, 115111 (2014).

[29] C. Fang, Y. Chen, H.-Y. Kee, and L. Fu, Topological nodal line semimetals with and without spin-orbital coupling, Phys. Rev. B **92**, 081201 (2015).

[30] Y. Kim, B. J. Wieder, C. L. Kane, and A. M. Rappe, Dirac line nodes in inversion-symmetric crystals, Phys. Rev. Lett. **115**, 036806 (2015).

[31] G. Bian, T.-R. Chang, R. Sankar, S.-Y. Xu, H. Zheng, T. Neupert, C.-K. Chiu, S.-M. Huang, G. Chang, I. Belopolski, *et al.*, Topological nodal-line fermions in spin-orbit metal $PbTaSe_2$, Nat. Commun. **7**, 10556 (2016).

[32] L. M. Schoop, M. N. Ali, C. Straßer, A. Topp, A. Varykhalov, D. Marchenko, V. Duppel, S. S. Parkin, B. V. Lotsch, and C. R. Ast, Dirac cone protected by non-symmorphic symmetry and three-dimensional dirac line node in ZrSiS, Nat. Commun. **7**, 11696 (2016).

[33] J. Hu, Z. Tang, J. Liu, X. Liu, Y. Zhu, D. Graf, K. Myhro, S. Tran, C. N. Lau, J. Wei, and Z. Mao, Evidence of topological nodal-line fermions in ZrSiSe and ZrSiTe, Phys. Rev. Lett. **117**, 016602 (2016).

[34] K. Manna, Y. Sun, L. Muechler, J. Kübler, and C. Felser, Heusler, Weyl and Berry, Nat. Rev. Mater. **3**, 244 (2018).

[35] E. Liu, Y. Sun, N. Kumar, L. Muechler, A. Sun, L. Jiao, S.-Y. Yang, D. Liu, A. Liang, Q. Xu, *et al.*, Giant anomalous Hall effect in a ferromagnetic kagome-lattice semimetal, Nature physics **14**, 1125 (2018).

[36] T. Graf, C. Felser, and S. S. Parkin, Simple rules for the understanding of Heusler compounds, Prog. Solid. State Ch. **39**, 1 (2011).

[37] C. Felser, L. Wollmann, S. Chadov, G. H. Fecher, and S. S. Parkin, Basics and prospective of magnetic Heusler compounds, APL materials **3**, 041518 (2015).

[38] C. Felser and A. Hirohata, *Heusler alloys* (Springer, 2015).

[39] G. Chang, S.-Y. Xu, H. Zheng, B. Singh, C.-H. Hsu, G. Bian, N. Alidoust, I. Belopolski, D. S. Sanchez, S. Zhang, *et al.*, Room-temperature magnetic topological Weyl fermion and nodal line semimetal states in half-metallic Heusler Co_2TiX (X= Si, Ge, or Sn), Sci. Rep. **6**, 38839 (2016).

[40] P. Li, J. Koo, W. Ning, J. Li, L. Miao, L. Min, Y. Zhu, Y. Wang, N. Alem, C.-X. Liu, *et al.*, Giant room temperature anomalous Hall effect and tunable topology in a ferromagnetic topological semimetal Co_2MnAl, Nat. Commun. **11**, 3476 (2020).

[41] A. Sakai, Y. P. Mizuta, A. A. Nugroho, R. Sihombing, T. Koretsune, M.-T. Suzuki, N. Takemori, R. Ishii, D. Nishio-Hamane, R. Arita, *et al.*, Giant anomalous nernst effect and quantum-critical scaling in a ferromagnetic semimetal, Nature Physics **14**, 1119 (2018).

[42] B. Bradlyn, L. Elcoro, J. Cano, M. Vergniory, Z. Wang, C. Felser, M. I. Aroyo, and B. A. Bernevig, Topological quantum chemistry, Nature **547**, 298 (2017).

[43] M. Vergniory, L. Elcoro, C. Felser, N. Regnault, B. A. Bernevig, and Z. Wang, A complete catalogue of high-quality topological materials, Nature **566**, 480 (2019).

[44] Y. Ji, W. Zhang, H. Zhang, and W. Zhang, Spin Hall conductivity and anomalous Hall conductivity in full Heusler compounds, New J. of Phys. **24**, 053027 (2022).

[45] P. Giannozzi, S. Baroni, N. Bonini, M. Calandra, R. Car, C. Cavazzoni, D. Ceresoli, G. L. Chiarotti, M. Cococcioni, I. Dabo, A. D. Corso, S. de Gironcoli, S. Fabris, G. Fratesi, R. Gebauer, U. Gerstmann, C. Gougoussis, A. Kokalj, M. Lazzeri, L. Martin-Samos, N. Marzari, F. Mauri, R. Mazzarello, S. Paolini, A. Pasquarello, L. Paulatto, C. Sbraccia, S. Scandolo, G. Sclauzero, A. P. Seitsonen, A. Smogunov, P. Umari, and R. M. Wentzcovitch, QUANTUM ESPRESSO: a modular and open-source software project for quantum simulations of materials, J. Phys. Condens. Matter **21**, 395502 (2009).

[46] D. R. Hamann, Optimized norm-conserving vanderbilt pseudopotentials, Phys. Rev. B **88**, 085117 (2013).

[47] J. P. Perdew, K. Burke, and M. Ernzerhof, Generalized gradient approximation made simple, Phys. Rev. Lett. **77**, 3865 (1996).

[48] N. Marzari and D. Vanderbilt, Maximally localized generalized Wannier functions for composite energy bands, Phys. Rev. B **56**, 12847 (1997).

[49] I. Souza, N. Marzari, and D. Vanderbilt, Maximally localized Wannier functions for entangled energy bands, Phys. Rev. B **65**, 035109 (2001).

[50] M. Gradhand, D. V. Fedorov, F. Pientka, P. Zahn, I. Mertig, and B. L. Györffy, J. Phys. Condens. Matter **24**, 213202 (2012).

[51] J. Noky, Q. Xu, C. Felser, and Y. Sun, Large anomalous Hall and Nernst effects from nodal line symmetry breaking in Fe_2MnX (X = P, As, Sb), Phys. Rev. B **99**, 165117 (2019).

[52] J. Noky, J. Gooth, C. Felser, and Y. Sun, Characterization of topological band structures away from the Fermi level by the anomalous Nernst effect, Phys. Rev. B **98**, 241106 (2018).

[53] B. Ernst, R. Sahoo, Y. Sun, J. Nayak, L. Müchler, A. K. Nayak, N. Kumar, J. Gayles, A. Markou, G. H. Fecher, and C. Felser, Anomalous Hall effect and the role of Berry curvature in Co_2TiSn Heusler films, Phys. Rev. B **100**, 054445 (2019).

[54] K. Manna, L. Muechler, T.-H. Kao, R. Stinshoff, Y. Zhang, J. Gooth, N. Kumar, G. Kreiner, K. Koepernik, R. Car, J. Kübler, G. H. Fecher, C. Shekhar, Y. Sun, and C. Felser, From colossal to zero: Controlling the anomalous Hall effect in magnetic Heusler compounds via Berry curvature design, Phys. Rev. X **8**, 041045 (2018).

[55] G. K. Shukla, A. K. Jena, N. Shahi, K. K. Dubey, I. Rajput, S. Baral, K. Yadav, K. Mukherjee, A. Lakhani, K. Carva, S.-C. Lee, S. Bhattacharjee, and S. Singh, Atomic disorder and Berry phase driven anomalous Hall effect in a Co_2FeAl Heusler compound, Phys. Rev. B **105**, 035124 (2022).

[56] V. T. N. Huyen, M.-t. Suzuki, K. Yamauchi, and T. Oguchi, Topology analysis for anomalous

Hall effect in the noncollinear antiferromagnetic states of Mn_3AN (A= Ni, Cu, Zn, Ga, Ge, Pd, In, Sn, Ir, Pt), Phys. Rev. B **100**, 094426 (2019).

[57] I. Samathrakis, N. Fortunato, H. K. Singh, C. Shen, and H. Zhang, Tunable anomalous Hall and Nernst effects in MM'X compounds, arXiv preprint arXiv:2207.03320 (2022).

[58] F. Mende, J. Noky, S. N. Guin, G. H. Fecher, K. Manna, P. Adler, W. Schnelle, Y. Sun, C. Fu, and C. Felser, Large anomalous Hall and Nernst effects in high Curie-temperature iron-based Heusler compounds, Adv. Sci. **8**, 2100782 (2021).

[59] T. Chen, T. Tomita, S. Minami, M. Fu, T. Koretsune, M. Kitatani, I. Muhammad, D. Nishio-Hamane, R. Ishii, F. Ishii, *et al.*, Anomalous transport due to Weyl fermions in the chiral antiferromagnets Mn_3X, X= Sn, Ge, Nat. commun. **12**, 572 (2021).

[60] Y. Wang, C. Xian, J. Wang, B. Liu, L. Ling, L. Zhang, L. Cao, Z. Qu, and Y. Xiong, Anisotropic anomalous Hall effect in triangular itinerant ferromagnet Fe_3GeTe_2, Phys. Rev. B **96**, 134428 (2017).

[61] M. Park, G. Han, and S. H. Rhim, Anomalous Hall effect in a compensated ferrimagnet: Symmetry analysis for Mn_3Al, Phys. Rev. Research **4**, 013215 (2022).

[62] T. Asaba, V. Ivanov, S. Thomas, S. Savrasov, J. Thompson, E. Bauer, and F. Ronning, Colossal anomalous Nernst effect in a correlated noncentrosymmetric kagome ferromagnet, Sci. Adv. **7**, eabf1467 (2021).

[63] T. Chen, S. Minami, A. Sakai, Y. Wang, Z. Feng, T. Nomoto, M. Hirayama, R. Ishii, T. Koretsune, R. Arita, *et al.*, Large anomalous Nernst effect and nodal plane in an iron-based kagome ferromagnet, Sci. Adv. **8**, eabk1480 (2022).